



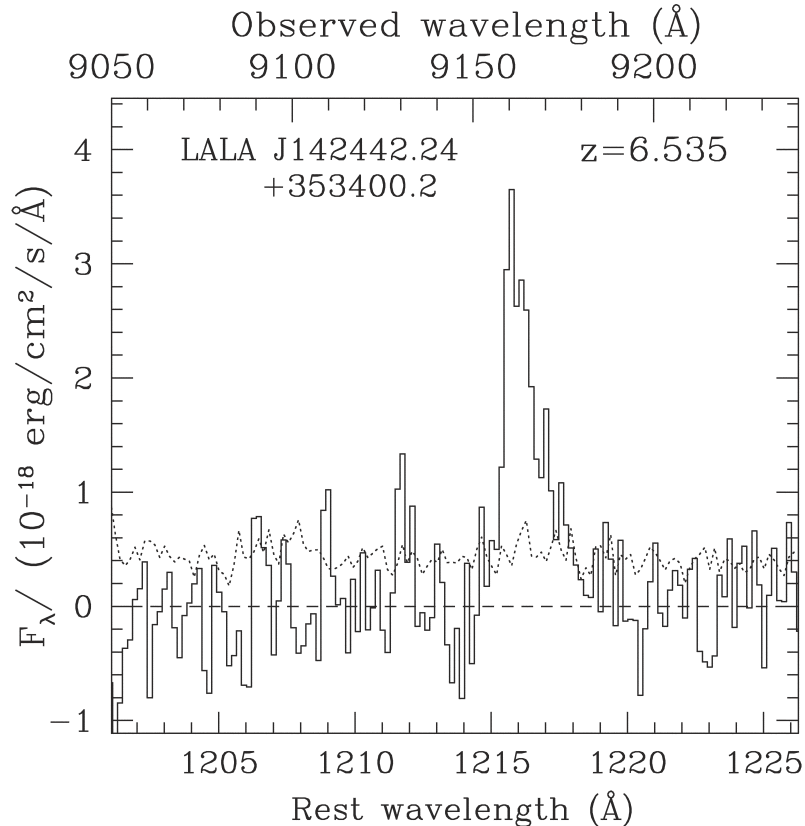
A Luminous Lyman- α Galaxy at $z=6.535$

Based on a contribution solicited from Sangeeta Malhotra & James Rhoads (Space Telescope Science Institute)

James Rhoads, Sangeeta Malhotra, and their collaborators have recently discovered a Lyman- α (Ly α) emitting galaxy at $z=6.535$ in the Large Area Lyman Alpha (LALA) survey at Kitt Peak. This galaxy, and the other results of this survey, may provide new insights into the nature of the reionization epoch in the very early universe.

The LALA survey identifies candidate Ly α -emitting galaxies based on wide-field imaging in a set of narrowband and broadband filters. Emission line candidates at $z=6.5$ were selected by comparing a 9200 \AA narrowband image with a continuum image obtained in the z' filter. Long exposures, made with the Mosaic I camera on the Mayall 4-m telescope, were needed to identify the galaxy at $z=6.535$; the 9200 \AA narrowband image has a total integration time of 28 hours. Blue continuum images from the NOAO Deep Wide Field survey (Dey and Jannuzi; www.noao.edu/noao/naoadeep) were used to distinguish high-redshift Ly α emitters from foreground [OII], [OIII], and Ha emitters. This strategy has proven successful in earlier LALA searches at $z=4.5$ (see the December 1999 NOAO/NSO Newsletter), and $z=5.7$.

These selection criteria yielded three $z=6.5$ candidates that were then studied spectroscopically with Gemini North + GMOS and/or Keck II + DEIMOS through time allocated by the NOAO Time Allocation Committee. Two of the three sources were confirmed as single, narrow emission line sources at wavelengths near 9160 \AA (source LALA J142442.24+353400.2) and 9136 \AA (source LALA J142441.20+353405.1). The line in LALA J142442.24+353400.2 shows all the hallmarks of high-redshift Ly α emission: large equivalent width (>530 \AA in the observer frame); a strong and statistically significant



Spectrum of LALA J142442.24+353400.2, obtained with the GMOS spectrograph on Gemini North in nod-and-shuffle mode. The net integration time was 5 hours. The solid histogram shows the measured flux; the dotted line shows the $1\text{-}\sigma$ flux uncertainties. The asymmetry of the line is clearly visible. There is no emission at 9072 \AA , where the [OIII]4959 line would be expected if the 9160 \AA feature were due to [OIII].

asymmetry; and a complete absence of other emission lines in the spectrum. This places it at $z=6.535$. The second object, LALA J142441.20+353405.1, is identified as an [OIII] emitter at $z=0.824$ based on a weak detection of the [OIII] 4959 \AA line in the Keck DEIMOS and Gemini GMOS spectra.

Given that only one $z=6.5$ source was found in one-third of a square-degree, the source likely corresponds to a high peak in the matter distribution: one object per survey volume roughly

matches the expected number density of $10^{11} M_{\odot}$ halos at $z=6.5$ in a Press-Schechter structure formation model.

The Ly α line in LALA J142442.24+353400.2 may have the highest luminosity and equivalent width yet found at $z=6.5$. The source SDF J132415.7+273058 (Kodaira et al. 2003) has about the same luminosity within the uncertainties, and an equivalent width near the $2\text{-}\sigma$ lower bound for LALA J142442.24+353400.2.) The luminosity

continued



A Luminous Lyman- α Galaxy continued

is 1.1×10^{43} ergs s^{-1} (using a cosmology with $\Omega_m = 0.27$, $\Omega_\Lambda = 0.73$, and $H_0 = 71$ km s^{-1} Mpc $^{-1}$). This implies a star formation rate of $>11 M_\odot$ yr $^{-1}$, assuming that the conversion between Ly α photons and star formation expected in the local universe holds also for this object.

The high Ly α luminosity and equivalent width suggest some interesting possibilities with regard to reionization. Because Ly α photons are resonantly scattered by neutral hydrogen, Ly α -emitting galaxies may suffer considerable attenuation of their line flux when embedded in a neutral intergalactic medium (IGM). Such an effect can be avoided only if the Ly α photons are substantially redshifted before encountering the IGM, either by redshifting in the Hubble flow while traversing their parent galaxy's Stromgren sphere (e.g., Rhoads and Malhotra 2001), or by some intrinsic

offset between the systemic velocity of the parent galaxy and the emitted line wavelength (e.g., Santos 2003).

The ionizing source in LALA-J142442.24+353400.2 should produce a Stromgren sphere $0.3 t_7^{1/3}$ Mpc in radius, given a lifetime for the ionizing source of $10^7 t_7$ yr, and would imply a line center optical depth $\tau \sim 4 t_7^{-1/3}$ due to the neutral IGM outside the Stromgren sphere. While the object could in principle occupy the Stromgren sphere of a brighter neighbor, any such neighbors ought to be detected in the LALA z' filter image, and none are observed.

In a neutral universe, a source like LALA J142442.24+353400.2 would require an intrinsic equivalent width $>120\text{\AA}$ even if the Ly α line is redshifted as suggested by Santos, and $>400\text{\AA}$ in the absence of such a redshift. The

former is consistent with the observed Ly α equivalent width distribution at $z=4.5$ (Malhotra and Rhoads 2002). The latter is high even for the $z=4.5$ sample. Thus, the properties of this object are most easily understood if the Universe is mostly ionized at $z=6.5$. The constraint on reionization may be refined through deeper broadband images of LALA J142442.24+353400.2 (which are planned with the Hubble Space Telescope and should replace the current lower bound on equivalent width with a firm measurement) and through future surveys that will yield statistical samples of Ly α galaxies at these redshifts.

These results have been accepted for publication in the *Astrophysical Journal*.

A Spectroscopic Survey for Superwinds in Massive Starbursts

David Rupke & Sylvain Veilleux (University of Maryland)

In recent years, mechanical feedback from star formation and active galactic nuclei has been hailed as a "miracle cure" to cosmology's ailments. Mechanical feedback may pollute and heat the intergalactic medium to observed levels, explain the mass-metallicity relation of ellipticals, account for the under-production of low-mass galaxies, and produce the Milky Way's baryon deficit.

Despite our increasing knowledge of galaxy-scale winds, the relationship between their properties and frequency of occurrence and the properties of the galaxies hosting these winds have yet to be established quantitatively. Such knowledge is important as the input to simulations of galaxy formation and evolution that incorporate these winds. Furthermore, superwinds have not been studied extensively outside of the local universe (except at very high redshift). Finally, we know little about winds in the most massive galaxies with the highest star formation rates.

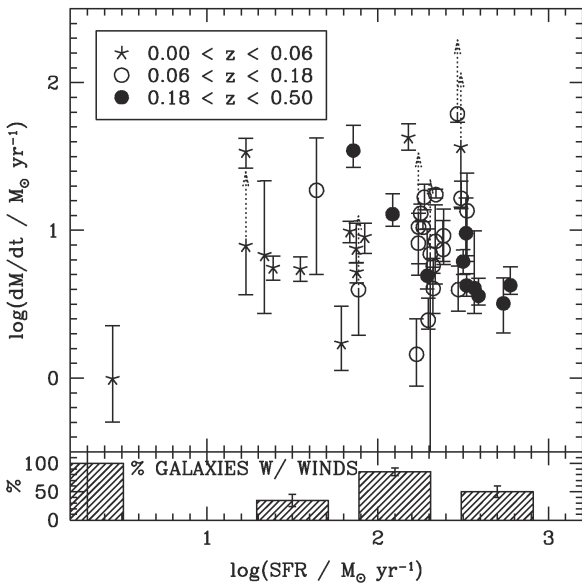
We are conducting a large survey of starburst-driven superwinds in over 75 galaxies, searching for statistical trends in wind properties as a function of host galaxy properties and redshift (Rupke, Veilleux, and Sanders 2002; Rupke, Veilleux, and Sanders 2004a,b, in preparation). Our galaxy sample consists of a large number of interacting galaxies with high star formation rates (ultraluminous infrared galaxies, or ULIRGs) with redshifts up to $z=0.5$, as well as a complementary sample of galaxies with lower star formation rates (leading to a dynamic range in star formation rate of two orders of magnitude).

To probe the properties of these winds, we use absorption-line spectroscopy of the NaI D $\lambda\lambda 5890, 5896$ doublet, which is conveniently located below 1 micron for galaxies with modest redshifts. This feature can be fitted with complex profiles to determine the outflow velocities and mass outflow rate in individual galaxies. Normalizing the mass outflow

continued



Superwinds in Massive Starbursts continued



Mass outflow rate (top) and wind detection frequency (bottom) as a function of star formation rate in our sample of starbursting infrared-luminous galaxies. There is no dependence of the mass outflow rate on the star formation rate. The different symbols represent different redshift bins and are labelled in the legend.

rate to the global star formation rate then yields a measure of the amount of interstellar gas entrained in the wind relative to the gas turned into stars (the “mass entrainment efficiency”). Over half of our data were obtained with the Kitt Peak 4-m using its workhorse spectrograph, the RC Spectrograph.

We find that superwinds are more common in ULIRGs (64% detection frequency) than in galaxies with lower star

formation rates (45%). The maximum velocities in the components that are outflowing are 325–425 km/s on average, with an upper limit of ~700 km/s. Significantly, these velocities are less than the (isothermal) escape velocity of a galaxy with $v_c=200\text{--}300$ km/s. We tentatively conclude that little of the cold, neutral material in these winds will escape the galaxy and enter the intergalactic medium. However, the hot gas in these winds (carrying much of the metallicity) will be more likely to escape.

The figure shows that the mass outflow rate in these galaxies is not correlated with the star formation rate. We also find that the mass entrainment efficiency for ULIRGs is much smaller than 1, is generally in the range 0.01–0.1, and is inversely proportional to star formation rate (SFR). The overall normalization of this quantity is somewhat uncertain given our lack of knowledge of the spatial extent of the absorbing gas and its geometry, but the dependence on SFR appears to be secure (unless the radius of the wind changes significantly with SFR).

Starbursts in ULIRGs are therefore much less efficient in powering massive superwinds than those in less-luminous galaxies. Why? One obvious possibility is the large concentrations of molecular gas in these galaxies, which may obstruct the winds. Secondly, radiative losses are likely to be significant in the denser environment of ULIRGs, therefore reducing the amount of energy available to drive the outflow.

A complete description of these data is forthcoming (Rupke, Veilleux, and Sanders 2004a,b in preparation), and the results derived from our sample of star-forming galaxies will be compared with those found in a large sample of infrared-luminous AGNs (Rupke, Veilleux, and Sanders 2004c, in preparation).

Faint Galaxy Counts and the Normalization of the Galaxy Luminosity Function

Seth Cohen (Arizona State University)

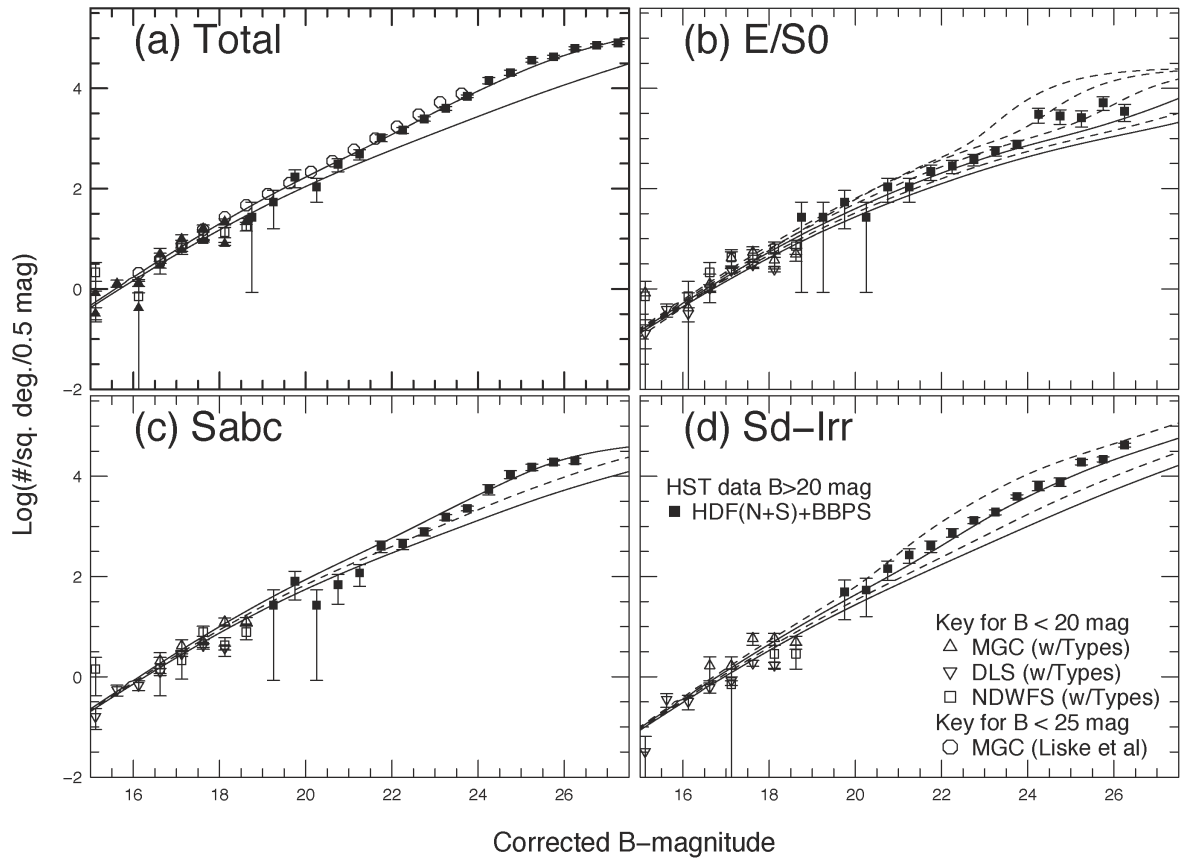
A major focus of the Hubble Space Telescope (HST) has been to study the morphology of faint galaxies and to relate apparent changes in the distributions of morphological types (over cosmic time) to physical processes such as star formation, luminosity evolution, and merging. An important result that has emerged is that most faint galaxies are not the classical ellipticals and spirals that dominate the galaxy population in the local universe.

Instead, the faint-blue galaxy (FBG) excess, detected in earlier ground-based surveys, was found to be composed of galaxies that have morphologies similar to local late-type spirals, irregulars, peculiars, and mergers. This FBG excess was an excess of the faint ($B>23\text{--}25$ mag) galaxy counts over the predictions of models that assumed no evolution in the local galaxy luminosity function (LF). In order for the models to match the observed galaxy counts,

continued



Faint Galaxy Counts continued



B-band galaxy counts as a function of morphological type. The models shown represent different amounts of luminosity evolution. The lower solid line is the nonevolving model and the upper solid line corresponds to luminosity evolving as $(1+z)^2$.

they had to be normalized by a factor of almost two at B=18 mag, regardless of the adopted cosmology. A group of us (Stephen Odewahn at McDonald Observatory, Rogier Windhorst at ASU, Simon Driver at RSAA/ANU, Jochen Liske at ESO, and I) have studied this normalization factor using both HST and ground-based data, investigating in particular the possible dependence of the normalization factor on morphological type.

The figure shows our results for the galaxy counts as a function of morphological type and B-band magnitude. The filled black squares are our combined results from HST using the Wide-Field and Planetary Camera 2 (WFPC2) surveys for the northern and southern Hubble Deep Fields and our own 30-field WFPC2 B-Band Parallel Survey. All of the HST galaxies have been classified into the three morphological classes shown using an automated artificial neural network galaxy classifier. The lower solid line is the nonevolving model, and the faint galaxy excess can be seen in all four panels of the plot. Also apparent from the plot

is that even with 30 WFPC2 fields, there are not enough bright galaxies to properly study the normalization issue at B=18 mag.

Fortunately, the average size of a galaxy at B=18 mag is about one arcsec, which is near the typical seeing limit that can be achieved with wide-field cameras from the ground. We utilized three publicly available ground-based surveys with deep wide-field images in the B-band with good seeing. We used four MOSAIC fields from the NOAO Deep-Wide Field Survey (NDWFS; Jannuzi & Dey), seven MOSAIC fields from the Deep Lens Survey (DLS; Tyson), and the 30 square degree Millennium Galaxy Catalog (MGC; Liske et al.). It was essential that we had the actual images so that we could measure their fluxes with the same software that we used for the HST work. Morphological types for the ground-based data were assigned by eye. The plot shows that the results from these three different surveys agree quite well with each other and line up nicely with the HST data.

continued



Faint Galaxy Counts continued

The plotted models use the measured type-dependent LF from Marzke et al. (1998), WMAP cosmology, type-dependent k -corrections, and they assume that luminosity evolves as a power law with redshift. The results are that ground-based data show *no need for a normalization factor* for any of the types or for the population as a whole. The best

fitting model (upper solid line) for all types is the one where luminosity evolves as $(1+z)^2$. There are some discrepancies, such as an excess of the Sd-Irr counts at the faint-end, and the Sabc counts at $B < 24$ mag. Since the median redshift at $B = 25$ mag is $z \approx 1.5$, this could indicate that the merger rate was higher in the past.

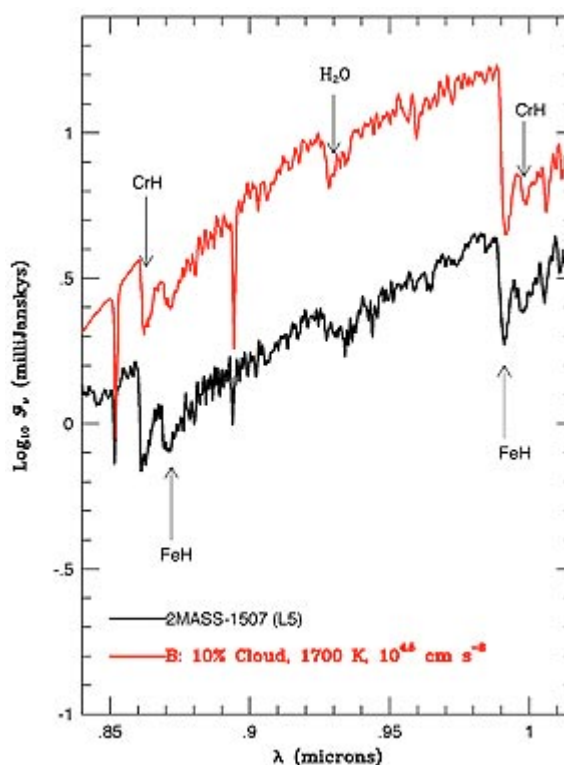
Metal Hydride Opacities in Brown Dwarfs

Mike Dulick (NSO), Adam Burrows (University of Arizona) & Peter Bernath (University of Waterloo)

With the discovery of the numerous L-type brown dwarfs, the transition-metal hydrides CrH and FeH have become crucial species for the identification of substellar objects. L-type dwarfs and the cooler T-type brown dwarfs bridge the gap in surface temperatures between Jupiter-like gaseous planets and M-type stars. Since the surface temperatures of these substellar objects fall below 2000K, with the exception of the strong atomic absorption lines from the alkali metals, the predominant spectral features are due in large part to absorption by molecular species such as H_2O , CO, CH_4 , CrH, and FeH.

The Wing-Ford band, which is the 0–0 vibrational band of the $F^4\Delta_i - X^4\Delta_i$ transition of FeH, makes its first appearance in late M-type stars and can also be seen in sunspots. M-type stars are characterized by strong TiO and VO bands, which fade as the photospheric temperature drops below 2000K for early L objects. L-type brown dwarfs are thus characterized by the absence of metal oxides and by the presence of the 0–0 (9896Å) and 1–0 (8691Å) bands of the $F^4\Delta_i - X^4\Delta_i$ transition of FeH and the 0–0 (8611Å) and 0–1 (9969Å) bands of the $A^6\Sigma^+ - X^6\Sigma^+$ transition of CrH. The simulation of the spectral energy distribution of L-type brown dwarfs requires the line positions and line strengths for these near-infrared transitions of FeH and CrH. Reliable thermochemistry is also needed (i.e., partition functions and the Gibbs free energy of formation as a function of temperature) to compute abundances and column densities.

Line lists for FeH and CrH were generated from the high-resolution Fourier transform laboratory spectra recorded at the National Solar Observatory's McMath-Pierce Solar Telescope Facility at Kitt Peak. Line positions were extrapolated to high J and v values using molecular constants. Line-strength factors were computed using the methods of *ab initio* quantum chemistry, and the thermochemistry was reevaluated. This information was then fed into a model for L-dwarf stars that basically starts by calculating the opacity (line strength integrated over radial absorption depth) as a function of temperature and pressure, incorporating all



Comparison of a measured opacity spectrum from an actual L5 dwarf, 2MASS-1507, with a synthetic spectrum using data for CrH and FeH. (Note: Calculated curve [red trace] is intentionally offset for display purposes.)

known species identified in L-dwarf spectra. The model then proceeds to adjust the effective temperature, gravity, and pressure along with the abundances of the species and a number of other important controlling factors, including the gravitational field and particle size associated with Mie scattering by mineral cloud formations, until agreement with the measured absolute flux density is achieved.

continued



Metal Hydride Opacities in Brown Dwarfs continued

Spectral information amassed from the analysis of laboratory metal-hydride spectra alone was insufficient in calculating line strengths, especially for temperatures up to 2000K. Calculating Einstein A-values for the rovibronic levels required supplemental information about the transition dipole moment function and the lower- and upper-state internuclear potentials for computing Franck-Condon factors. In principle, this information could have been furnished by radiative lifetime measurements and inversion of the rovibrational levels using the Rydberg-Klein-Rees method. The obstacles associated with making such measurements and the lack of sufficient vibrational information from the spectra made it more attractive to obtain this missing information directly from high-level *ab initio* calculations. Usage of experimental data for determining line strengths was restricted to calculating Hönl-London factors that reflect the actual electronic coupling in these rovibronic levels. In addition, these

theoretical calculations also provided essential information about the low-lying electronic states with energies up to 10,000 cm⁻¹ above the ground states, which made it possible to calculate the partition function for temperatures up to 2000K, especially for FeH.

A comparison of a measured opacity spectrum from an actual L5 dwarf, 2MASS-1507 (see figure), recorded in the region from 0.84 to 1.2 μm at a resolving power of 1000, with a synthetic spectrum using the generated data for CrH and FeH, gave remarkably good agreement. This was achieved through minimal adjustment in the effective temperature, gravity, and particle size of the mineral cloud.

For detailed information, see C. W. Bauschlicher et al., *J. Chem. Phys.* 115, 1312 (2001); A. Burrows et al. *ApJ*, 577, 986 (2002); and M. Dulick et al., *ApJ*, 594, 651 (2003).

Predicting the Maximum of Solar Activity with NSO Coronal Data

Dick Altrock (Air Force Research Lab)

Prediction of the exact date of the maximum of the 11-year solar activity cycle is controversial among solar scientists and of some importance to satellite operators, space-system designers, etc. Most predictions are based on physical conditions occurring at or before the solar-cycle minimum preceding the maximum in question. However, another indicator of the timing of the maximum occurs early in the rise phase of the solar cycle.

Scans of the solar corona at 0.15 solar radii above the visible edge, or limb, of the Sun in the spectral line of 13-times-ionized iron (Fe XIV) at 530.3 nm have been obtained since 1973 with the photoelectric coronal photometer at the John W. Evans Solar Facility of the National Solar Observatory at Sacramento Peak. Early in the solar cycle, high-latitude coronal emission features appear and begin to move toward the poles. This motion is maintained for a period of three or four years, at which time the features disappear near the poles. This phenomenon, called the "Rush to the Poles," was first identified in polar-crown prominences, and has been used to invent a new method for predicting the date of the maximum of the solar cycle.

Figure 1 shows the Rush to the Poles for solar cycles 21 and 22. The slopes of the Rush to the Poles in cycles 21 and 22 are measured to be 8.11° per year and 11.32° per

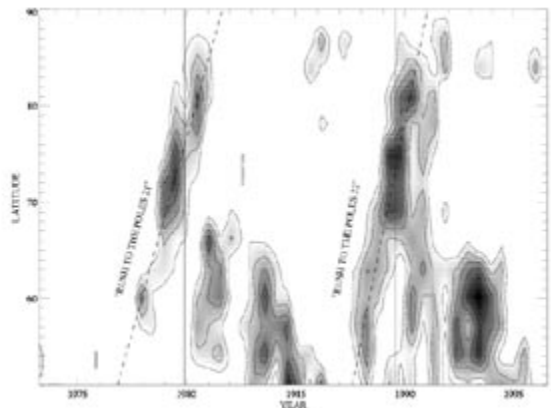


Figure 1. Contours of the north-plus-south average of 189-day averages (seven 27-day rotation periods or approximately six months) of the density of local intensity maxima of all usable Fe XIV 530.3 nm 1.15 solar-radii scans for solar activity cycles 21 and 22, isolated for latitudes above 51°. The linear fits to the Rush to the Poles are shown as dashed lines. The vertical lines show the dates of solar maxima, as defined by the sunspot number.

continued



Predicting the Maximum of Solar Activity continued

year, respectively, for an average of $9.72^\circ \pm 1.61^\circ$ per year. The extrapolated fit to the Rush to the Poles for these cycles reaches the poles on 1981.64 and 1991.04, or 1.74 and 1.44 years after solar maximum, respectively, yielding an average lag of 1.59 ± 0.15 years.

In 1997, Fe XIV emission features began to move toward the poles. To predict the date of maximum for solar cycle 23 we use the above slopes and estimate that the Rush to the Poles began on 1997.58 at 54° latitude (see figure 2). The extrapolation from that point would reach the poles between 2000.76 and 2002.02. If we then apply the above lags, we would find the cycle 23 maximum occurring between 1999.32 and 2000.28, for an average of 1999.80 ± 0.48 . Actual cycle 23 maximum occurred at 2000.3.

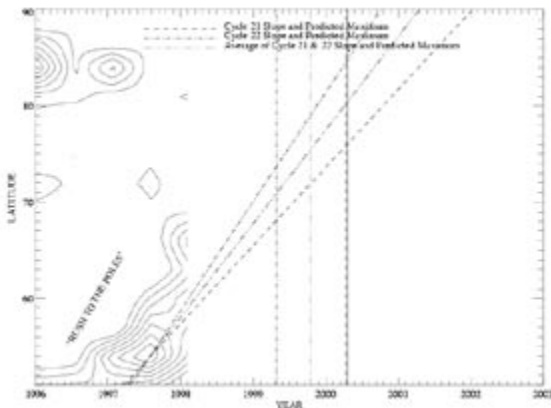


Figure 2. The predicted coronal Rush to the Poles for solar cycle 23 using data through July 1997 and fits from cycles 21 and 22. Vertical lines are the predicted and actual (solid line) dates of solar maximum.

The error in the predicted date of solar-cycle-23 maximum was -0.50 ± 0.48 years. This prediction could have been made 2.7 years ahead of solar maximum, which is only 1.2 years after the preceding solar minimum. Thus, this method is competitive with other methods for determining the date of solar maximum. Including more data as the cycle progresses does not improve the accuracy of the prediction.

For solar cycle 24, a prediction of the date of solar maximum can be made when the Rush to the Poles becomes apparent, approximately 11 years after its cycle-23 onset on 1997.58, or in 2008 or 2009. When that occurs, the average slope for cycles 21 through 23, $9.38^\circ \pm 1.71^\circ$ per year, can be used to predict the arrival date at the poles of the Rush to the Poles, and then the average lag, 1.52 ± 0.20 years, can be used to predict the date of solar maximum.

This work is supported by the Air Force Office of Scientific Research.

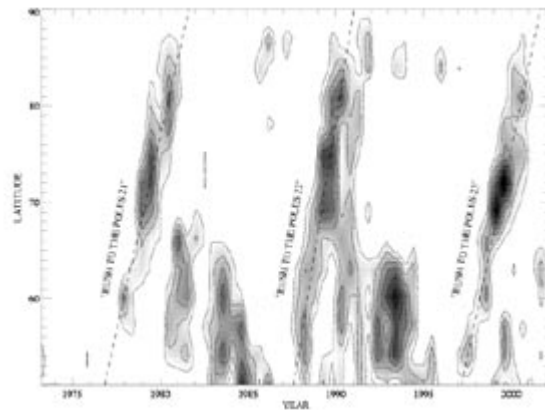


Figure 3. Fits to the coronal Rush to the Poles for solar cycles 21, 22, and 23.